

Microstructure Evolution and Mechanical Properties of cp-Ti Processed by a Novel Technique of Rotational Constrained Bending



T. KRAJŇÁK, M. JANEČEK, P. MINÁRIK, J. VESELÝ, P. CEJPEK, J. GUBICZA, P.T. HUNG, D. PREISLER, F. NOVÝ, A.G. RAAB, G.I. RAAB, and R. ASFANDIYAROV

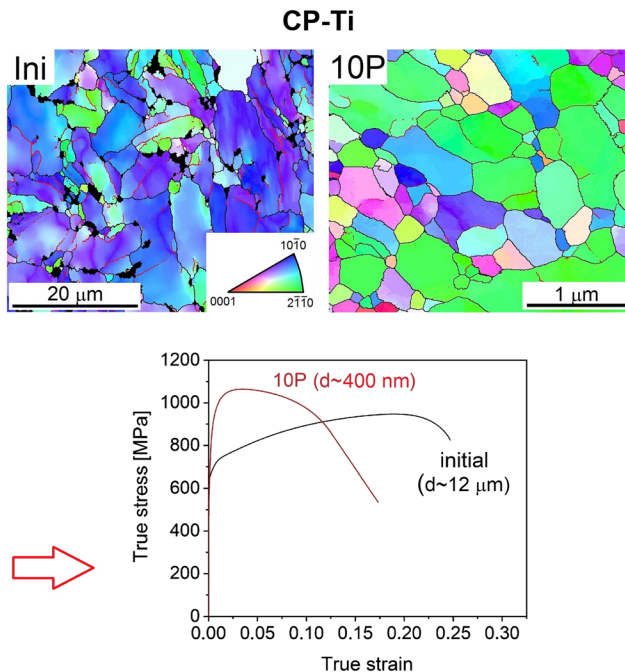
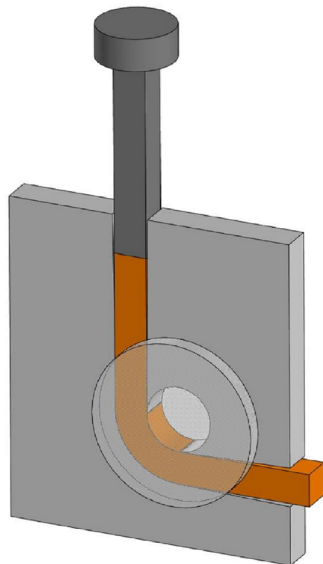
In this study, a novel severe plastic deformation technique referred to as rotational constrained bending (RCB) is introduced. A special constrained bending die, which imposes bending deformation to the billet during the first pass, was developed for repetitive processing of pre-extruded commercially pure Ti. Strain-induced microstructural changes were investigated by a special technique of automated crystal orientation mapping in TEM simultaneously with advanced X-ray line profile analysis. Plastic deformation distribution, imposed to the billets after a selected number of passes, was followed by precise microhardness mapping. Exceptional microstructure refinement was attained by the application of repetitive bending deformation. Average grain size decreased down to 400 nm, and the dislocation density increased by about 35 pct after ten passes. X-ray macrotexture measurements revealed the formation of a basal slip texture component commonly observed in HCP materials processed by equal channel angular pressing; however, exceeding four passes, a strong $\{11\bar{2}0\}$ fiber texture started to form. Mechanical testing in tension showed a significant increase in strength in the RCB-processed samples. The proof-stress and tensile strength increased by 30 and 15 pct after four passes, respectively. At a higher number of passes, the proof stress slightly decreased because of the texture softening.

T. KRAJŇÁK, M. JANEČEK, P. MINÁRIK, J. VESELÝ, P. CEJPEK, D. PREISLER, and F. NOVÝ are with the Faculty of Mathematics and Physics, Charles University, Ke Karlovu 3, 121 16 Praha 2, Czech Republic. Contact e-mail: tom.krajnak@gmail.com J. GUBICZA and P.T. HUNG are with the Department of Materials Physics, Eötvös Loránd University, P.O.B. 32, Budapest 1518, Hungary. A.G. RAAB and G.I. RAAB are with the Ufa State Aviation Technical University, 12 K. Marx str., Ufa, Russian Federation, 450008. R. ASFANDIYAROV is with the Ufa State Aviation Technical University and also with the Institute of Molecule and Crystal Physics UFRC RAS, 151 pr. Oktyabrya, Ufa, Russian Federation, 450075

Manuscript submitted August 26, 2020, January 7, 2021.

Article published online March 3, 2021

Rotational constrained bending



<https://doi.org/10.1007/s11661-021-06157-0>

© The Minerals, Metals & Materials Society and ASM International 2021

I. INTRODUCTION

ATTRACTIVE mechanical and other physical properties of metals having a refined microstructure led to the improvement or modification of classical metal-forming processes and to the development of new techniques of material preparation. It is well known that ultrafine-grained or even nano-grained materials may be prepared by two fundamentally different procedures, which are referred to as the “top-down” and “bottom-up” approaches.^[1–3] One of the widely used techniques employing the “top-down” approach, *i.e.*, the initial coarse-grained material is gradually refined, is the method of severe plastic deformation (SPD).^[4,5] In this technique, extremely high plastic deformation is imposed on the material under high hydrostatic pressure. The isostatic pressure is formed when the materials are processed through a special die, that preserves the original dimension and shape of the sample. Significant grain refinement for a wide range of materials having BCC, FCC and HCP crystal structures was achieved by processing *via* SPD techniques.^[6–8] Nevertheless, the wider practical utilization of traditional SPD techniques such as high-pressure torsion (HPT)^[9] or equal channel angular pressing (ECAP)^[10] is hindered because of the relatively small size of the processed samples. In this regard, the new techniques of continuous HPT,^[11] ECAP-Conform^[12] or I-ECAP,^[13] developed in the last decade, seem to be very promising. ECAP-Conform enables processing of long billets.

Nevertheless, the strong frictional forces acting during processing consume a lot of energy, which causes the processing to be energetically inefficient. Moreover, due to the high friction forces, the processing of high-strength materials is very challenging.

In recent years, Raab *et al.* developed a new technique of severe plastic deformation, based on the repetitive bending of the material, which should eliminate the above-mentioned issues.^[14] In this technique, the material in the form of a long bar is bent by 90 deg in the set

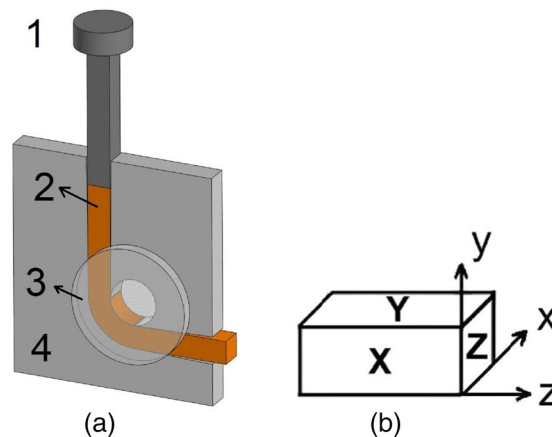


Fig. 1—(a) Design of the die for processing *via* RCB (1: plunger, 2: billet, 3: driving roller, 4: die) and (b) notation of the axes and planes in the sample coordinate system.

of rollers that form a channel. Processing by so-called “free bending in rotating rollers” imposes tensile deformation (outer part) and compression deformation (inner part) of the cross section of the sample. The processing between driving or non-driving rollers significantly reduces friction forces, which enables processing of a wider range of materials and processing at higher rates compared to the other SPD techniques.^[15] Despite the reduced friction forces, the processing of “hard” materials such as titanium cannot be processed by free bending. In this regard, the present article focuses on commercially pure Ti processed by a slightly modified laboratory die, under the condition of the constrained bending, which enables employing a hydraulic machine for sample processing. This method is referred to as rotational constrained bending (RCB). Such geometry produces a hydrostatic pressure during material processing. The main objective of the article was to investigate the strain distribution imposed during successive passes of cp-Ti through the constrained bending die and to describe in detail the strain-induced microstructure changes and the resulting mechanical properties.

II. EXPERIMENTAL PROCEDURE

Commercially pure Ti (grade 4) was supplied in the form of extruded bars. Billets with a square cross section of $9 \times 9 \text{ mm}^2$ and a length of 80 mm were successfully processed by the RCB method at $300 \text{ }^\circ\text{C}$, using a pressing velocity of 6 mm/s, up to a total of ten passes following the Bc route (*i.e.*, the sample is rotated by 90 deg around the processing direction after each pass). The strain imposed to the billet per pass was found inhomogeneous throughout the billet cross section.^[16] To investigate the microstructure evolution with an increasing number of passes in detail, a series of samples after one, two, four, eight and ten passes was prepared. The samples were processed through the die schematically shown in Figure 1(a). In this die, the sample is

bent by 90 deg while passing through the channel delimited from the bottom side by a solid block and from the top part by a driving roller. Deformation hardening in the cross section was investigated in detail by microhardness mapping using a regular network consisting of > 900 indents. Microhardness measurement under an applied load of 500 g and a dwell time of 10 seconds was performed by the automatic microhardness tester Qnes Q10a. Comprehensive microstructure characterization (except the samples processed by one and ten passes where the top, bottom and central parts were investigated) was performed in the central parts of the samples cross section. Jeol 2200FS transmission electron microscopes (TEM) operated at 200 kV and a FEI Quanta 200 scanning electron microscope (SEM) operated at 10 kV and equipped with an EDAX electron backscatter diffraction (EBSD) camera were used for microstructure investigations (the step size of EBSD scans was 100 nm). Measured EBSD and ACOM-TEM data were cleaned and evaluated by TSL OIM Analysis 7 software. The average grain size evaluated by this software is specified by grain diameter. The diameter of a particular grain was calculated by determining the area of a grain and then assuming the grain is a circle. The average grain size was then calculated using area fraction statistic. Only grains separated by high-angle grain boundaries were considered in the grain size calculation. Dislocation density and macrotexture were measured utilizing X-ray diffraction (XRD). The X-ray diffraction spectra were recorded using the high-resolution rotating anode diffractometer Rigaku RAmultiMax9 using $\text{CuK}\alpha_1$ (wavelength: $\lambda = 0.15406 \text{ nm}$) radiation. A narrow parallel X-ray beam with a size of $2 \times 0.2 \text{ mm}^2$ was used in the experiments. The X-ray line profile analysis (XPLA) was performed by the Convolutional Multiple Whole Profile (CMWP) fitting method.^[17] The instrumental broadening was neglected during the fitting of XRD patterns because of very broad peaks. The macroscopic crystallographic texture was measured in the central part of the cross section. The measurement of pole figures for reflections (0002),

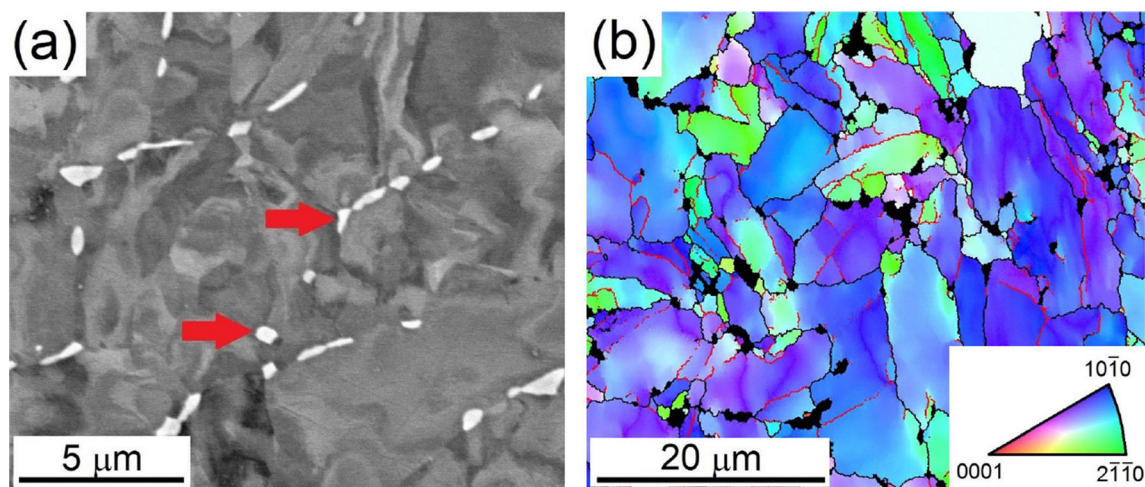


Fig. 2—(a) SEM micrograph and (b) inverse pole figure map of cp-Ti in the initial state. The light gray areas indicated by red arrows in (a) and the black areas in (b) are secondary beta-Ti particles.

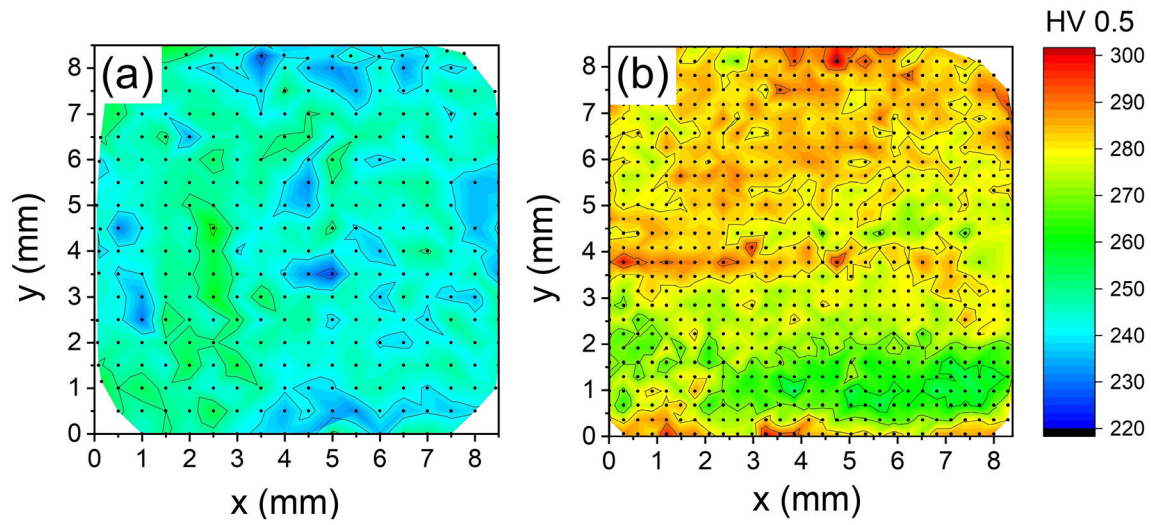


Fig. 3—Microhardness maps of (a) the initial state and (b) the sample after the first pass measured on the cross section.

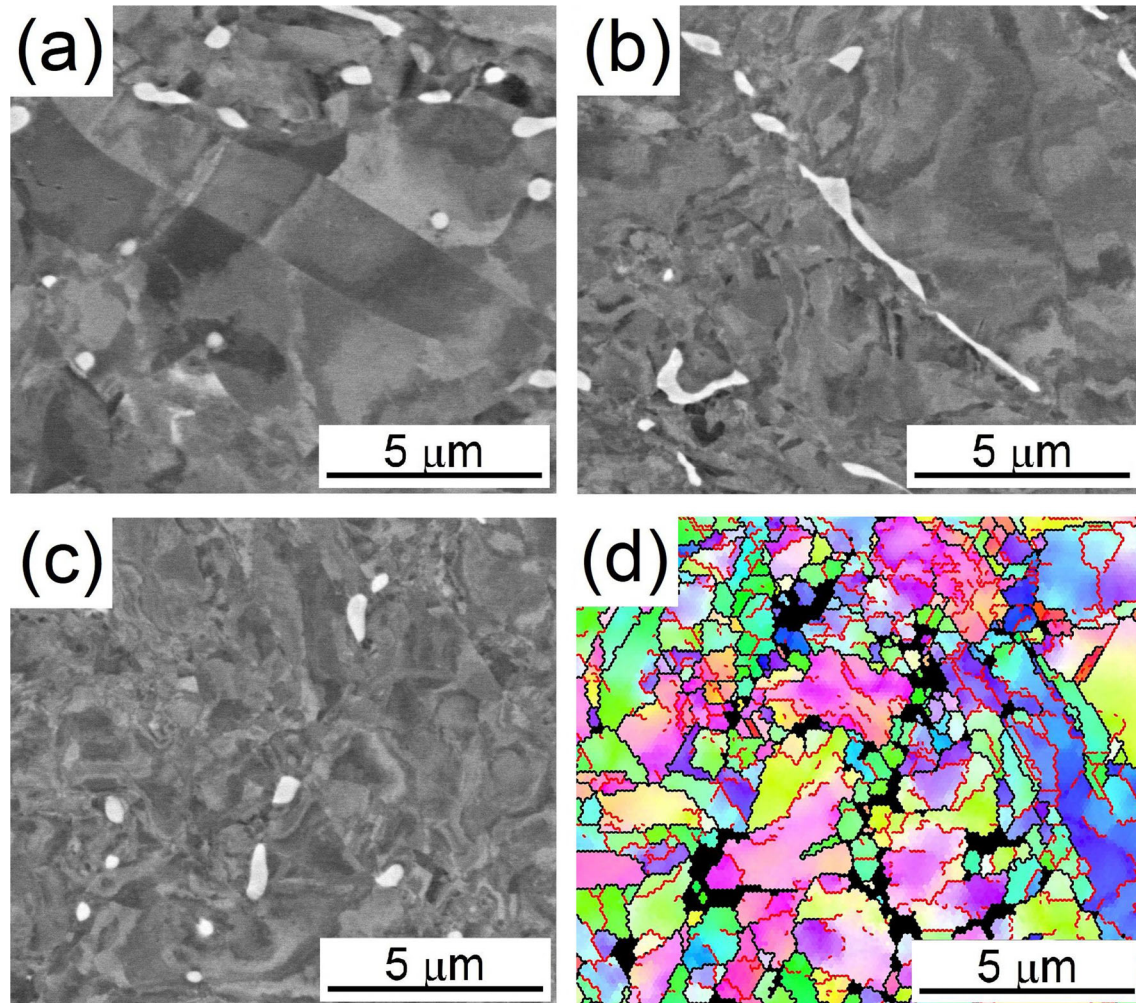


Fig. 4—SEM micrographs of the sample after the first pass from (a) the bottom, (b) the middle and (c) the top of the cross section, (d) the inverse pole figure map from the top area.

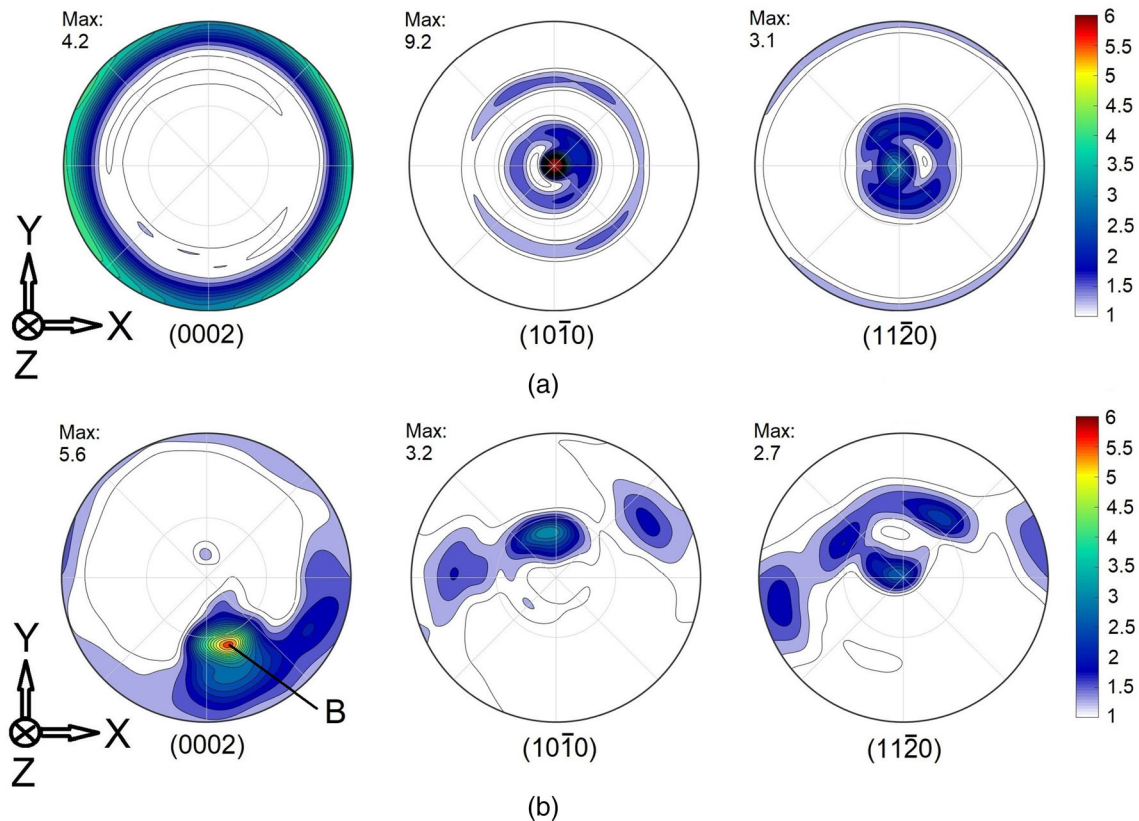


Fig. 5—(0002), (10 $\bar{1}$ 0) and (11 $\bar{2}$ 0) XRD pole figures of (a) the initial state and (b) the sample after the first pass of RCB.

(10 $\bar{1}$ 0), (10 $\bar{1}$ 1), (10 $\bar{1}$ 3) and (11 $\bar{2}$ 2) was performed on a Philips X'Pert PRO MRD X-ray diffractometer with an Eulerian cradle, using CuK α radiation ($\lambda = 0.15418$ nm). The configuration of optics was the following: polycapillary and cross slits in the primary beam and the plan-parallel collimator with 0.27 deg slit, 0.04 rad Soller slits and carbon monochromator in the diffracted beam. The orientation distribution function (ODF) calculation and plotting of recalculated pole figures were performed by MTEX software.^[18] The samples for microstructure investigations were first ground using 1200-, 2400- and 4000-grit SiC papers and then polished by colloidal alumina and silica suspensions with decreasing particle size down to 0.04 μm for 16 hours using a vibratory polisher. For XLPAs, the polished surface was additionally etched using Kroll's reagent consisting of 100 ml water, 3 ml hydrofluoric acid and 6 ml nitric acid for 1 minute. Disks with a diameter of 3 mm for TEM were first mechanically ground to a thickness of about 120 μm and subsequently twin jet electropolished in the solution of 6 pct HClO $_4$ and 33 pct butyl alcohol in methanol at the temperature of -20 °C. Mechanical testing at room temperature was performed by tension with the initial strain rate of 10^{-3} s $^{-1}$ using an INSTRON ElectroPuls 10000 testing instrument. Dog-bone shaped samples with a gauge length of 12 mm and a width of 3 mm were used. The tensile axis of the samples was parallel to the longitudinal axis of the RCB-processed billets. The orthogonal sample

coordinate system (x -, y -, z -axes) and corresponding perpendicular planes X , Y and Z used for the representation of microhardness and texture measurements are depicted in Figure 1(b). The z -axis is parallel to the pressing direction of the processed sample.

III. EXPERIMENTAL RESULTS

A. Microstructure of the Initial State and the Sample After the First Pass

The microstructure of the commercial pure Ti processed by extrusion (initial condition) consists of heavily deformed alpha grains and secondary phase particles (highlighted by red arrows in Figure 2(a)) distributed primarily at the grain boundaries (Figure 2(b)) in which black spots correspond to these particles. These secondary particles containing iron (confirmed by the EDS analysis) could be referred to as beta phase.^[19] The average grain size evaluated from the EBSD map is about 12 μm .

Microstructure changes introduced by a single pass of constrained bending were investigated by precise microhardness (HV) measurement across the cross and longitudinal section of individual samples. Figure 3 shows the Vickers microhardness map of the initial condition and the specimen processed by a single pass. The variations of microhardness across the cross section of the billets are clearly displayed by the color code in

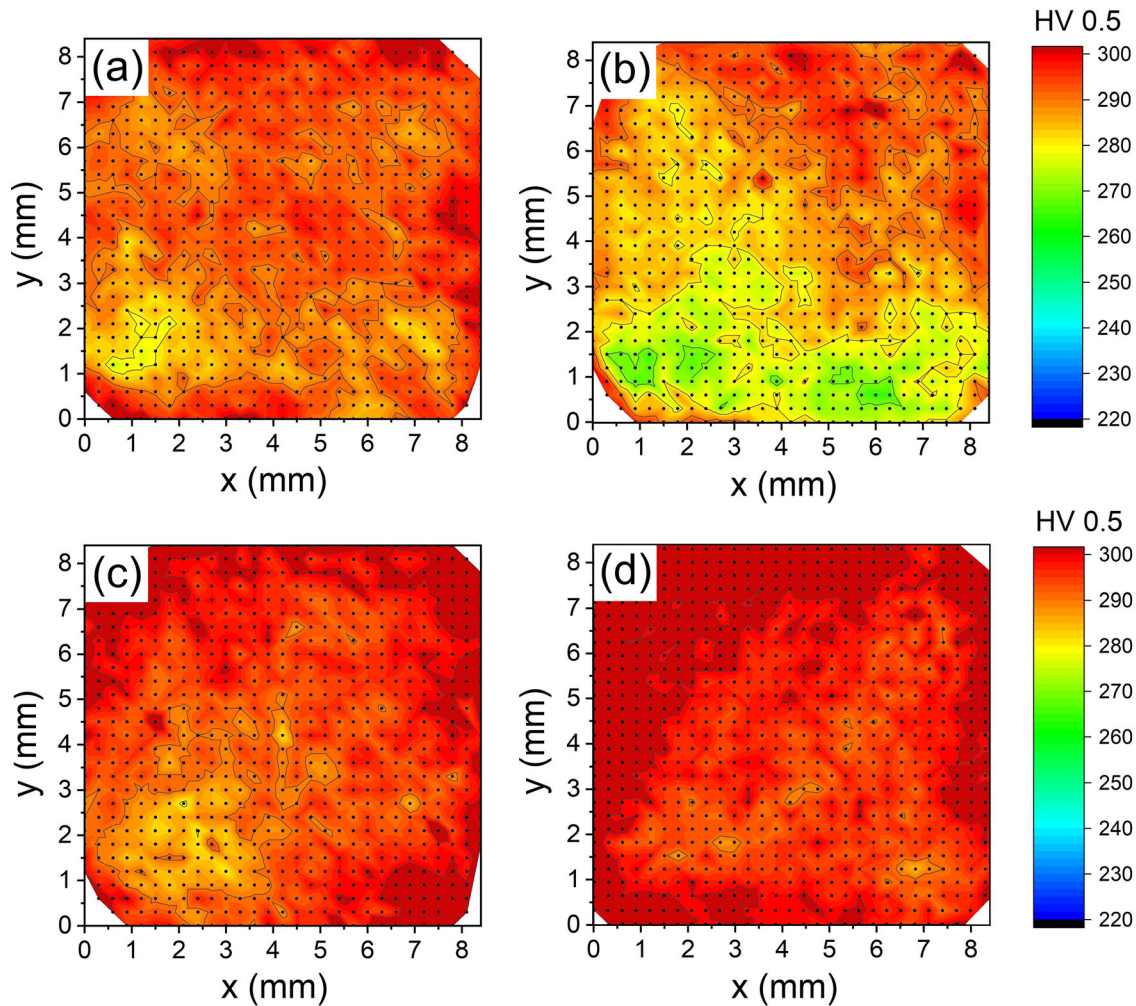


Fig. 6—Microhardness maps measured on the cross section of cp-Ti samples processed by (a) two, (b) four, (c) eight and (d) ten passes of RCB. The black dots inside the maps represent positions of individual indents.

these maps. Even after the first pass, a significant increase of the microhardness mainly at the top of the billet can be observed. HV gradually decreases towards the bottom part. The overall increase in the microhardness in the top and bottom parts is about 20 and 10 pct compared to the initial sample, respectively. Similar results were found also in the longitudinal section (not shown here). Moreover, some inhomogeneity in the microhardness values was observed along the length of the billet (along the z -axis). Non-homogeneous distribution of HV in the cross section of the single pass (1P) sample indicates the presence of a gradient type microstructure. Representative SEM micrographs from the different areas of the cross section of the sample after the first pass are shown in Figure 4. Consistent with increasing HV, a gradual refinement of the microstructure from the bottom to the top part was observed. Figure 4(b) captures the transition between the initial and the refined microstructures in the central region of the sample. Detailed EBSD investigation in the top part revealed the presence of new grains separated by high-angle grain boundaries (HAGBs, for which the misorientation is > 15 deg, highlighted by black color)

alongside with the heavily deformed pre-existing grains characterized by misorientation variation within their interiors. These grains contain a high fraction of low-angle grain boundaries (LAGBs for which the misorientation is in the range of 5 to 15 deg) highlighted by red color in Figure 4(d).

Figure 5 shows that the microstructure of the initial state exhibits a strong $\{10\bar{1}0\}/\{11\bar{2}0\}$ fiber texture, typical for hexagonal materials processed by hot extrusion.^[20] After the first pass, the initial texture was considerably modified. The new strong texture maximum tilted by about 45 deg toward the pressing direction (z -axis) is present on the basal (0002) pole figure (Figure 5). This texture component denoted as B was defined in Reference 21 and corresponds to an extensive activation of basal slip during processing.

B. Evolution of the Microstructure with Increasing Number of Passes

Vickers microhardness maps of the cp-Ti samples processed by different numbers of passes are shown in Figure 6. After the second pass, substantial hardening is

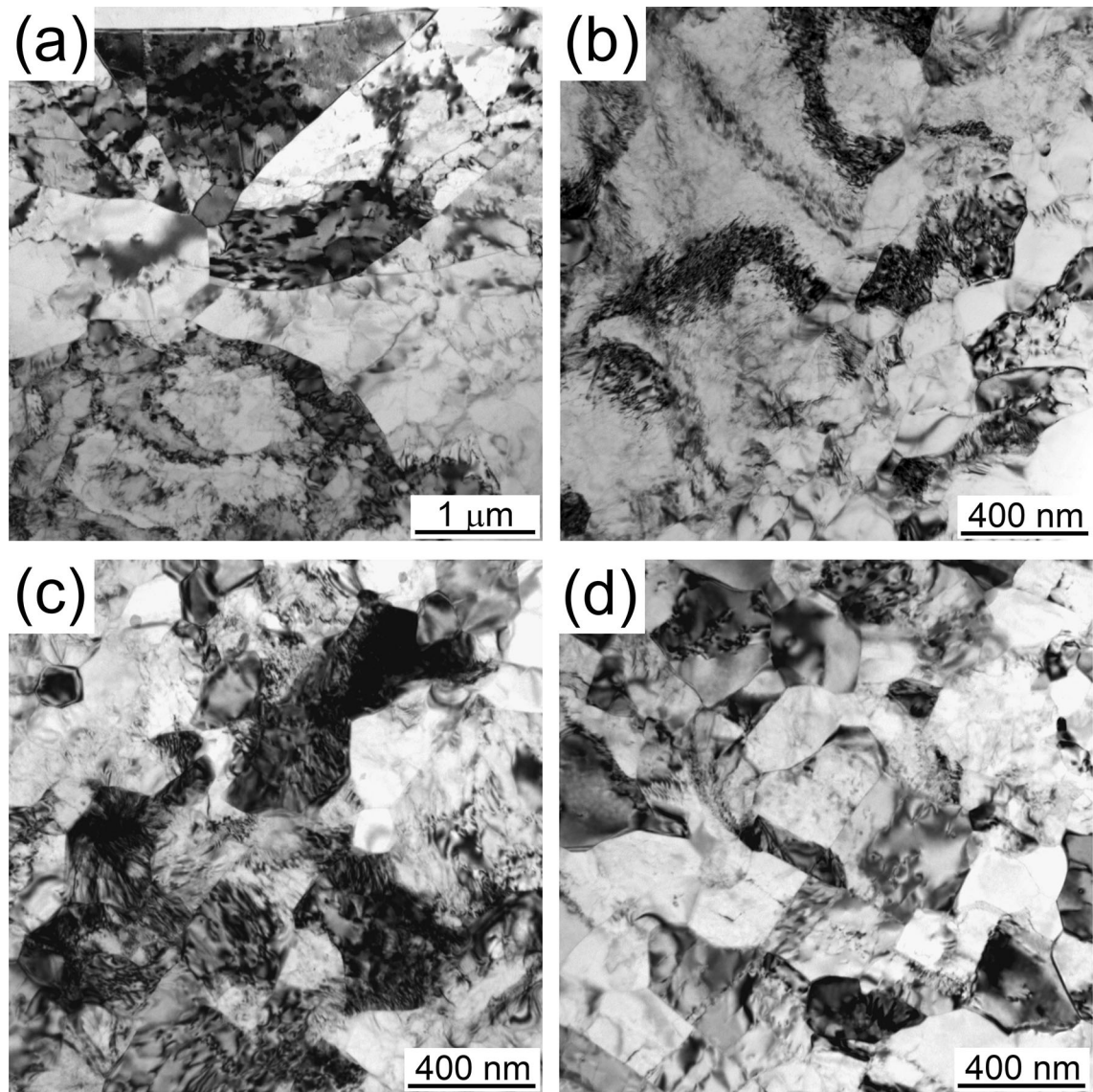


Fig. 7—Bright-field TEM micrographs of cp-Ti (a) in the initial state and after (b) two, (c) eight and (d) ten passes of RCB.

spread into the upper right area of the cross section as a consequence of rotating the sample by 90 deg. Due to this rotation, the top part, already hardened after the first pass is flipped to the right side and the left side of the original IP sample (top part during the second pass) undergoes an additional hardening during the second pass. In this way, the heterogeneous distribution of HV observed after the first pass was gradually transformed to a uniform one in the whole cross section of the billets after ten passes.

Microstructural observations performed by TEM in the central part of the cross section revealed a gradual microstructure refinement up to ten passes (Figure 7). Whereas the microstructure after two and four passes (not shown here) is bimodal and contains original extruded grains and areas of new small equiaxed grains the microstructure after eight passes is refined and consists of heavily deformed grains containing high dislocation density. On the other hand, a partially

recovered microstructure, consisting of equiaxed grains is apparent after ten passes. Microstructure homogeneity of the sample after ten passes was confirmed by TEM observation in the peripheral area of the cross section, where no difference from the central part was observed. Besides the observations in the bright field, the special technique of automated crystal orientation mapping in TEM (ACOM-TEM^[22]) was also used. This method allows the identification of the crystallographic orientation of grains with sizes down to around 10 nm, which is well below the limit of EBSD resolution. Moreover, the average grain size and the fraction of HAGBs and LAGBs can be extracted from the measured inverse pole figure (IPF) maps. Figure 8 shows the IPF maps for the samples after two and ten passes obtained by ACOM-TEM. The fraction of the very fine grains separated by HAGBs (highlighted by black color) significantly increases after ten passes; nevertheless, some LAGBs (highlighted by red color) are still present. This indicates

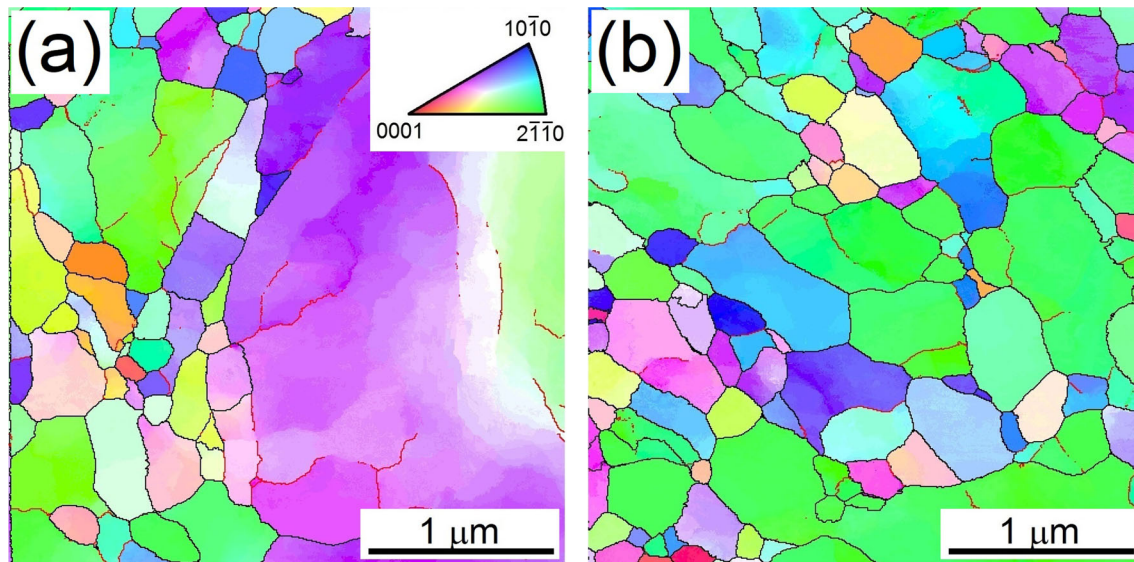


Fig. 8—Inverse pole figure maps of cp-Ti after (a) two and (b) ten passes of RCB (ACOM-TEM). LAGBs and HAGBs are marked by red and black colors, respectively.

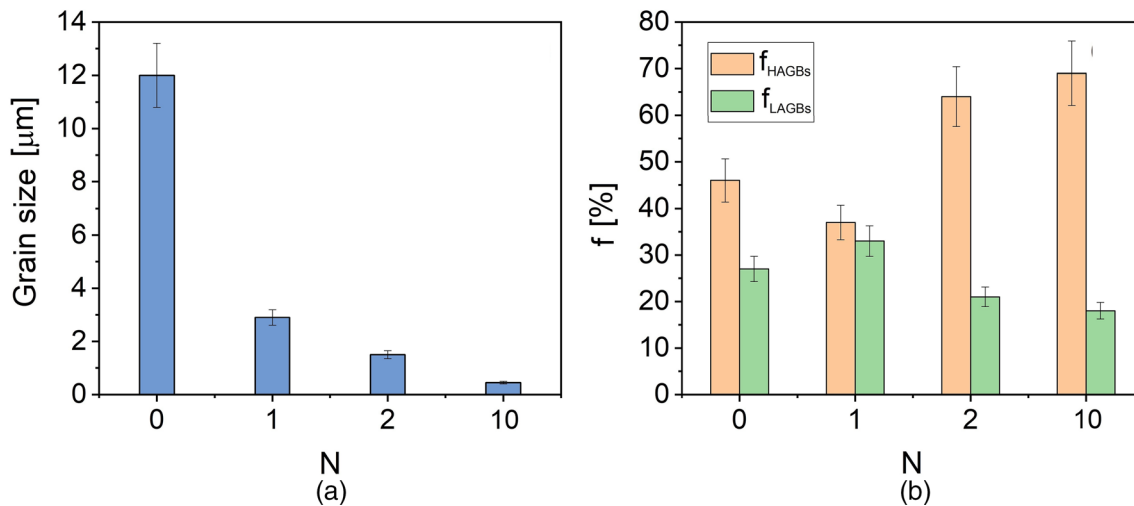


Fig. 9—(a) Average grain size and (b) fraction of HAGBs and LAGBs for selected samples.

that the fraction of HAGBs has not reached the saturated value yet. Moreover, the similar color of the grains in these maps indicates the presence of crystallographic texture in both samples. Figure 9(a) summarizes the microstructural parameters evaluated from both EBSD and ACOM-TEM measurements on selected samples. As Figure 9(a) shows, the area-weighted mean grain size rapidly decreases after two consecutive passes from the initial value of 12 μm down to the 1.5 μm. Further straining up to ten passes decreases the grain size only moderately and the average grain size further decreases to 400 nm. It should be noted that only grains separated by HAGBs were considered in the grain size calculation. On the other hand, the fraction of HAGBs dropped after the first pass. Further processing gradually increased the fraction

of HAGBs. In the case of LAGBs, the opposite trend to that of HAGBs was observed. After a total of 10 passes the fraction of HAGBs and LAGBs was 70 and 18 pct, respectively.

Macrottexture investigation in the central region of the cross section utilizing XRD showed further texture transformation at a higher number of passes. As it is apparent from the basal (0002) pole figures, after two passes the texture component B is additionally tilted roughly by 45 deg towards the *x*-axis. With the subsequent processing, the position of component B remains fixed; nevertheless, its intensity gradually decreases until it completely disappears after ten passes. On the other hand, formation and strengthening of the {11-20} fiber component parallel with the *z*-direction are

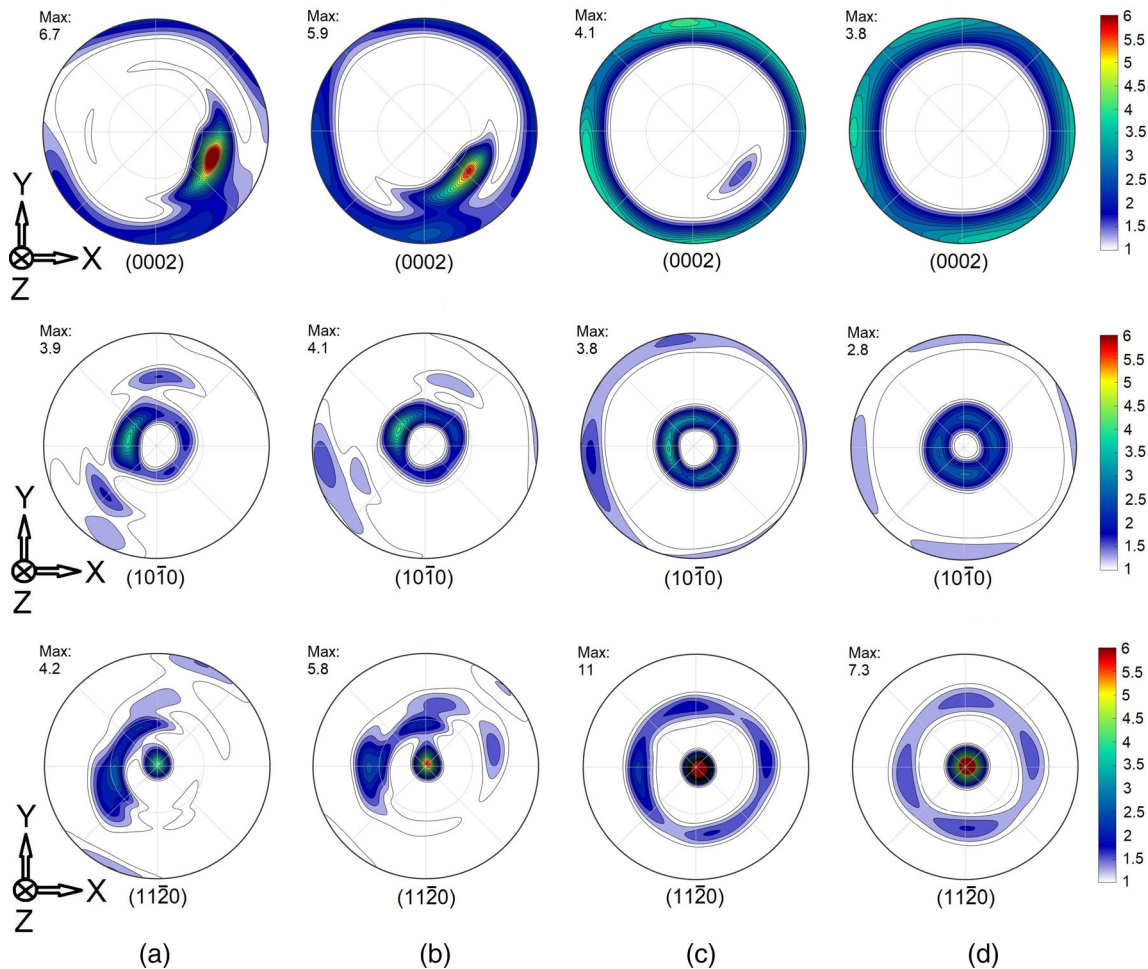


Fig. 10—(0002), $(10\bar{1}0)$ and $(11\bar{2}0)$ XRD pole figures for the samples processed by (a) two, (b) four, (c) eight and (d) ten passes of RCB measured in the central part of the cross section.

clearly seen from Figure 10. Eventually, this component became dominant after the final step of the processing.

The dislocation density (ρ) and crystallite size were evaluated from the peak broadening of the XRD profiles using the CMWP method. The dislocation arrangement parameter (M) was determined from the peak shape in the tail part. The area-weighted mean crystallite size ($\langle x \rangle_{\text{area}}$) was calculated from the median (m) and the variance (σ) of the log-normal size distribution.^[17] The evolution of the dislocation density with an increasing number of passes (N) is plotted in Figure 11(a). The dislocation density increases up to two passes and drops after four passes. During further straining, the dislocation density remains almost constant, with only a slight decrease after ten passes. The sample processed by two passes exhibits about two times higher dislocation density ($\sim 10 \times 10^{14} \text{ m}^{-2}$) compared to the initial state ($\sim 5 \times 10^{14} \text{ m}^{-2}$). As Figure 11(b) shows, the crystallite size (the size of coherently scattering domains) decreased already after the first pass from ~ 100 to ~ 70 nm and remained almost constant during further straining. The crystallite size slightly decreased between eight and ten passes. The measured values of ρ and $\langle x \rangle_{\text{area}}$ are listed in Table I. The dislocation

arrangement parameter as a function of the number of passes is plotted in Figure 11(c). The parameter M , reflecting the strength of the dipole character of dislocations, reached the maximum after eight passes. On the other hand, the value of parameter M after ten passes is comparable to the initial state. The lower value of parameter M in both aforementioned samples indicates a stronger screening of strain fields of dislocations due to their arrangement into low-energy configurations, such as dipoles or low-angle grain boundaries compared to the other RCB-processed samples.

C. Mechanical Properties

The average microhardness calculated for the central part of the cross section (area $3 \times 3 \text{ mm}^2$) as a function of N is plotted in Figure 12. The average microhardness increased with an increasing number of passes. However, the microhardness increased significantly after the first pass, while during further straining only a moderate increase in the HV was observed. The microhardness increased from ~ 245 HV (initial state) to about 300 HV ($N = 10$).

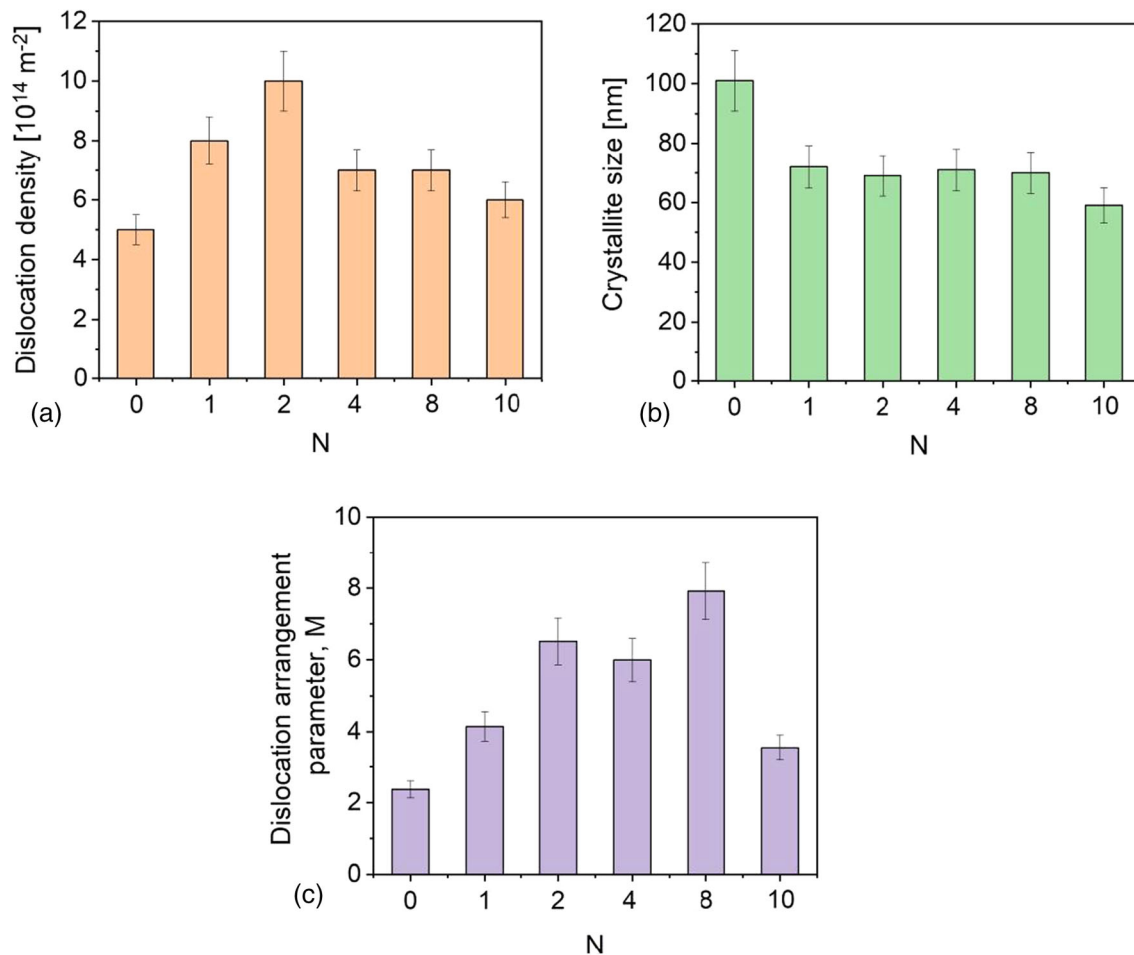


Fig. 11—(a) Evolution of the dislocation density, (b) the crystallite size and (c) the dislocation arrangement parameter M with an increasing number of passes obtained from XLPAs.

Table I. The Values of the Proof Stress ($\sigma_{0.2}$), Tensile Strength (σ_{\max}) Evaluated from the True Stress–True Strain Curves and Values of the Dislocation Density (ρ) and Crystallite Size ($\langle x \rangle_{\text{area}}$) Obtained from XLPAs

Number of Passes	$\sigma_{0.2}$ [MPa]	σ_{\max} [MPa]	$\rho[10^{14} \text{ m}^{-2}]$	$\langle x \rangle_{\text{area}}$ [nm]
0	643 ± 23	928 ± 26	5 ± 1	101 ± 10
1	718 ± 21	890 ± 33	8 ± 1	72 ± 7
2	762 ± 10	930 ± 2	10 ± 1	69 ± 7
4	845 ± 13	1060 ± 43	7 ± 1	71 ± 7
8	758 ± 21	1040 ± 38	7 ± 1	70 ± 7
10	757 ± 5	1058 ± 7	6 ± 1	59 ± 6

The error of the tensile parameters was calculated as the standard deviation.

Besides the microhardness measurements, the cp-Ti samples were also deformed in tension at room temperature. The representative true stress–true strain curves of the initial state and the samples processed by RCB are plotted in Figure 13(a). The evolution of the proof stress $\sigma_{0.2}$ and the tensile strength σ_{\max} with an increasing number of passes is shown in Figure 13(b). The measured values of the tensile parameters are summarized in Table I. The tensile strength σ_{\max} is highlighted by the black star on the individual tensile curves.

The RCB processing significantly increases the strength of cp-Ti, while the ductility decreases markedly. The proof stress first increases up to four passes (an increase by 30 pct compared to the initial state is observed) and then drops after eight passes. After further processing up to ten passes, the value of the proof stress remains constant. On the other hand, the tensile strength decreases slightly after the first pass and then gradually increases after further processing. From the fourth pass, the tensile strength remained constant

within an experimental error and reached the maximum value of 1060 MPa (about 15 pct higher compared to the initial state). In the initial state, significant work hardening can be observed before reaching σ_{\max} . On the other hand, samples processed by constrained bending exhibit a high strain hardening rate already after the yield point up to the strain of about 0.04 followed by gradual softening during further straining (except for the 1P sample, where hardening was observed up to the strain of 0.07).

IV. DISCUSSION

A. Microstructure Evolution and Mechanism of Grain Refinement

The microstructure observations presented above revealed that repetitive processing of cp-Ti in bending *via* the RCB technique resulted in a strong refinement of the initial extruded structure, texture modification and increase of dislocation density. As Figure 3(b) shows,

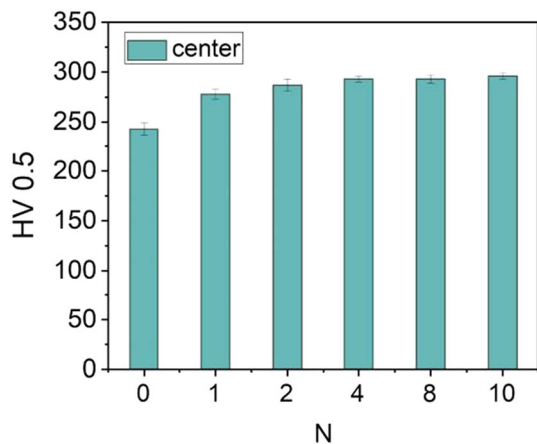
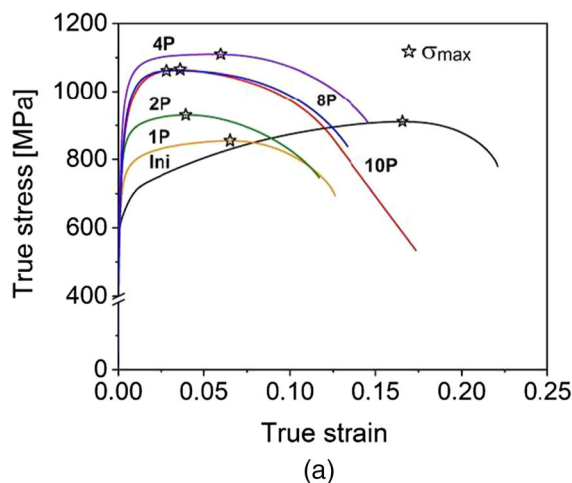


Fig. 12—The average microhardness as a function of the number of passes (N) calculated for the central part of the cross section.



the deformation imposed on the material by a single pass of RCB is not uniform. The upper part of the cross section (deformed by compression) exhibits higher microhardness compared to the bottom part of the cross section (deformed by tension), indicating the higher value of plastic deformation imposed to the top part compared to the bottom part. This is consistent with numerical simulations of strain distributions in CuZr alloy deformed in bending.^[23] Apart from the differences in the imposed strain in the top and bottom parts of the billet, partial inhomogeneity in the imposed strain was observed along the length of the billet. Such inhomogeneities in the imposed plastic deformation after the first pass can be removed by employing higher numbers of passes (Figure 6). By rotating the sample by 90 deg after each pressing, the strong deformation is imposed into all four corners of the square billet cross section after four passes, which speeds up the homogenization of the imposed plastic strain in the volume of the material. Nevertheless, the uniform microhardness values in the whole billet cross section were obtained only after ten passes. Direct microstructure observations indicate that with an increasing number of passes, the microstructure refinement is gradually spread to the whole volume of the material and proceeds from the edge part to the central part of the cross section. Whereas new refined grains separated by HAGBs were observed after the first pass in the upper part of the billet only (Figure 4(d)), after two passes these small grains appeared also in the central part of the cross section (Figure 8). During further processing, the number of small grains increases and the bimodal grain size distribution in the 2P sample is continuously transformed into a unimodal one. Final processing by ten passes results in a fully refined and homogeneous microstructure in the whole cross section. The original grain size of $\sim 12 \mu\text{m}$ decreased down to $\sim 400 \text{ nm}$, which is comparable to the cp-Ti processed by the commonly used ECAP technique.^[24–26]

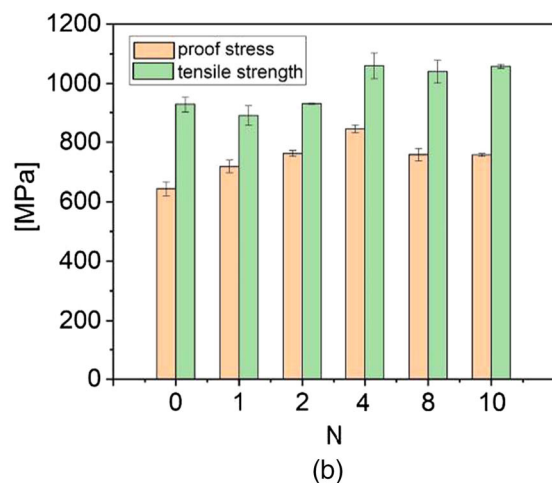


Fig. 13—(a) The true stress–true strain curves and (b) evolution of the proof stress $\sigma_{0.2}$ and the tensile strength σ_{\max} with a increasing number of passes. Each value represents an average of three tensile tests.

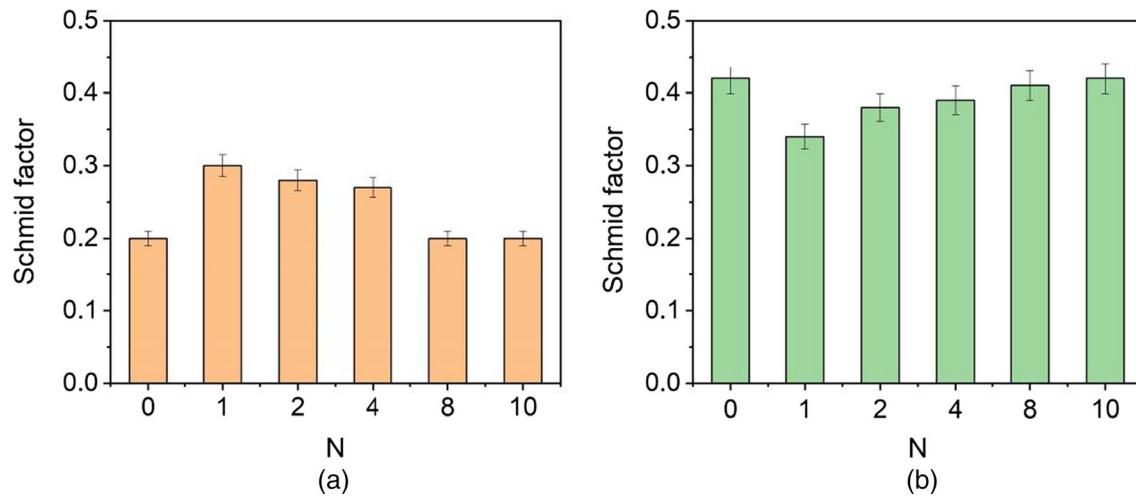


Fig. 14—Schmid factor for (a) (0001) $\langle 11\bar{2}0 \rangle$ basal and (b) (10 $\bar{1}0$) $\langle 11\bar{2}0 \rangle$ prismatic slip systems as a function of the number of passes.

Microstructure refinement in pure Ti processed by the ECAP technique was found to be driven by dynamic recovery and twinning.^[27,28] As the twinning activity in titanium usually decreases with decreasing grain size, massive twinning during ECAP processing takes place only during the first few passes until the grain size decreases to a critical size.^[29] Thus, dynamic recovery becomes the pre dominant refinement mechanism at a higher number of passes. Dislocations induced by deformation are accumulated in the grain interiors and rearranged to form low-angle grain boundaries, *i.e.*, dislocation walls or subgrain boundaries. During further straining, the misorientation across these boundaries increases and LAGBs gradually transform to HAGBs, which results in the formation of new small grains separated by HAGBs. Microstructural features of dynamic recovery were observed in the present study already after the first pass of free bending, when the fraction of LAGBs increased compared to the initial state (Figure 9(b)). Numerous LAGBs formed inside the pre-existing grains (Figure 4(d)). These boundaries divided the large grains into smaller parts. In some places, the LAGBs were already transformed to HAGBs, and new, fine equiaxed grains were present. Moreover, color variation inside the pre-existing grains indicated different misorientations, which are the driving force for dynamic recovery.^[30] On the other hand, microstructure refinement *via* twinning was not observed. This observation can be attributed to the small initial grain size of about 12 μm . Further accumulation of dislocations during subsequent passes leads to the gradual formation of new LAGBs in the non-fragmented areas and simultaneously to the transformation of existing LAGBs to HAGBs. Nevertheless, the process of microstructure refinement was not completed after ten passes. Some LAGBs, that did not fully transform to HAGBs, were still present (Figure 8).

Apart from the microstructure refinement, processing by RCB significantly increases the dislocation density. Dislocation density evaluated by XLPAs includes dislocations in grain and subgrain interiors as well as in

dislocation cell/subgrain boundaries and LAGBs. Thus, the increment of dislocation density during the early stages of RCB processing up to two passes can be ascribed to both the non-arranged dislocations stored in the grain interiors and the dislocations arranged into dislocation cells and LAGBs. Because of the increased fraction of non-arranged dislocations inside the grains, the parameter M increases up to two passes. The massive transformation of LAGBs to HAGBs between two and four passes effectively decreases the overall dislocation density (Figure 11(a)). While between four and eight passes, the dislocation density remains unchanged, the parameter M considerably increases and reaches a maximum value. This indicates that a partial decrease of dislocation density previously present in LAGBs is compensated by an increase of non-arranged dislocations. Consistently, numerous grains containing a high fraction of dislocations in the grain interiors are observed in the sample after eight passes (Figure 7). An additional decrease of dislocation density after ten passes can be attributed to dynamic recovery. As a result, dislocation density inside the grains significantly decreases. This is consistent with the reduced value of parameter M and the presence of numerous recrystallized grains almost free of dislocations observed in the microstructure after ten passes compared to eight passes. This clearly documents the benefit of using the combination of direct microstructure observations by TEM and indirect XLPAs for the characterization of microstructure evolution in cp-Ti processed by RCB.

B. Texture Evolution

Macrottexture investigations in Figure 10 indicated a gradual transformation of the original extruded texture during RCB. An evenly distributed maximum around the edge of pole figure (0002) was partially transformed to a strong texture component B tilted by 45 deg towards the x -axis after four passes. This texture is also formed during ECAP processing of materials with HCP crystal structure *via* the Bc route when the basal planes

are orientated parallel to the shearing plane.^[31,32] Rotation of basal planes is caused by the activation of basal slip during processing as was first proposed by Mukai *et al.*^[33] and experimentally confirmed by Krajník *et al.*^[31] The intensity of texture component B in the AX41 magnesium alloy processed by ECAP at 250 °C increased with an increasing number of ECAP passes because of the increasing activity of the basal slip. This result is in contrast to the constrained bending processing where the intensity of texture component B above four passes starts to weaken abruptly. This effect can be ascribed to the decreasing activity of the basal slip during free bending processing.

C. Mechanical Properties

In contrast to the gradual microstructure refinement which continues up to ten passes, the strength of the constrained bent samples changes non-monotonously. It differs from the cp-Ti processed by ECAP, where the gradual increase of the proof stress with an increasing number of passes was observed.^[25] The proof stress of the samples processed by RCB gradually increases up to four passes and drops after eight passes despite the continuing grain refinement. Such a drop can be attributed to the texture change, which occurs after four passes (Figure 10). To quantify the influence of the texture on the proof stress, the Schmid factors for uniaxial tension parallel to z -axis for (0001) $\langle 11\bar{2}0 \rangle$ basal and (10 $\bar{1}0$) $\langle 1120 \rangle$ prismatic slip systems were calculated from the experimentally measured texture using the MTEX software. As Figure 14 shows, the Schmid factor for the basal slip drops after eight passes and remains constant up to ten passes, while the Schmid factor for the prismatic slip slightly increases up to ten passes. The resulting texture change leads to a suppressed activation of a “harder” basal slip and enhanced activation of a “softer” prismatic slip, which effectively decreases the proof stress over four passes. Alongside the increasing value of the proof stress, the standard deviation decreases up to four passes, indicating a gradual homogenization of the mechanical properties in the whole volume of the material. After four passes, the maximum proof and tensile strength values are 845 MPa and 1060 MPa, respectively, which are comparable with the strength values of the most commonly used coarse-grained Ti-6Al-4V alloy, where $\sigma_{0.2}$ and σ_{\max} of 860 and 943 MPa were reported, respectively.^[34] In contrast to the proof stress, the microhardness continuously increased during RCB up to ten passes, consistent with the grain size refinement. This phenomenon can be explained by the fact that microhardness test introduces multiaxial loading compared to the uniaxial loading during the tensile test, and the influence of texture on the HV is partially suppressed. This result confirms the fact that the texture softening observed indeed affects the value of the proof stress at a higher number of passes. The significant texture softening that deteriorated the value of proof stress was also observed in AX41 magnesium alloy processed by ECAP.^[21]

The lack of strain hardening observed on the tensile curves in Figure 13(a), when the strain exceeds 0.05, is a significant feature of the stress–strain curves of nanostructured cp-Ti.^[35] It can be attributed to the small sizes of grains, subgrains and dislocation cells as well as to the high dislocation density stored in the processed material.^[36] When the stored dislocation density approaches the saturated value, the majority of the additional dislocations generated during tensile testing are annihilated or disappear into the sinks that are abundant in a material with such ultrafine-grained structures. Thus, further straining does not contribute to work hardening as dislocation generation and recovery are in a dynamic balance, and no significant change in dislocation density occurs.^[37]

V. CONCLUSIONS

CP-Ti samples were successfully processed by rotational constrained bending. The influence of the increasing number of passes on the strain distribution, microstructure evolution and mechanical properties was studied. The following conclusions can be drawn from this investigation:

- The heterogeneous distribution of the hardness after the first pass was continuously transformed to a uniform one in the whole cross section of the billets after ten passes.
- Rotational constrained bending was found to be effective for substantial microstructure refinement in commercially pure Ti.
- Fully refined homogenous microstructure with an average grain size about 400 nm was observed after ten passes.
- Apart from the significant microstructure refinement, a substantial increase in the dislocation density and a gradual transformation of the extruded texture were observed with the increasing number of passes.
- RCB resulted in the formation of two texture components, namely a basal slip texture component commonly observed in HCP materials processed by equal channel angular pressing and a $\{11\bar{2}0\}$ fiber component parallel to the z -direction. The increasing number of RCB passes resulted in a continuous suppression of the basal slip and the strengthening of the $\{11\bar{2}0\}$ fiber component until it became the only texture component after ten passes.
- Processing by constrained bending significantly increased both the microhardness and the strength of commercially pure Ti. The proof stress increased from 640 MPa (initial state) to about 850 MPa ($N = 4$).

ACKNOWLEDGMENTS

This work was financially supported by the Ministry of Education, Youth and Sports of the Czech Republic under the project LTARF18010 and by the

Ministry of Science and Higher Education of the Russian Federation under grant agreement no. 14.586.21.0059 (UIN: RFMEFI58618X0059). Partial financial support by ERDF project no. CZ.02.1.01/0.0/0.0/15_003/0000485 is also gratefully acknowledged. This work was supported in part by the Ministry of Human Capacities of Hungary within the ELTE University Excellence program (1783-3/2018/FEKUTSRAT).

REFERENCES

1. Y.T. Zhu, T.C. Lowe, and T.G. Langdon: *Scripta Mater.*, 2004, vol. 51, pp. 825–30.
2. D.B. Witkin and E.J. Lavernia: *Prog. Mater. Sci.*, 2006, vol. 51, pp. 1–60.
3. H. Gleiter: *Prog. Mater. Sci.*, 1989, vol. 33, pp. 223–15.
4. R.Z. Valiev, R.K. Islimgaliev, and I.V. Alexandrov: *Prog. Mater. Sci.*, 2000, vol. 45, pp. 103–89.
5. T.G. Langdon: *Acta Mat.*, 2013, vol. 61, pp. 7035–59.
6. J. Čížek, M. Janeček, T. Krajňák, J. Stráská, P. Hruška, J. Gubicza, and H.S. Kim: *Acta Mat.*, 2016, vol. 105, pp. 258–72.
7. Y. Duan, L. Tang, G. Xu, Y. Deng, and Z. Yin: *J. Alloys Compd.*, 2016, vol. 664, pp. 518–29.
8. J. Stráská, M. Janeček, J. Gubicza, T. Krajňák, E.Y. Yoon, and H.S. Kim: *Mater. Sci. Eng. A*, 2015, vol. 625, pp. 98–106.
9. A.P. Zhilyaev and T.G. Langdon: *Prog. Mater. Sci.*, 2008, vol. 53, pp. 893–79.
10. V.M. Segal: *Mater. Sci. Eng. A*, 1995, vol. 197, pp. 57–164.
11. K. Edalati and Z. Horita: *J. Mater. Sci.*, 2010, vol. 45, pp. 4578–82.
12. G.J. Raab, R.Z. Valiev, T.C. Lowe, and Y.T. Zhu: *Mater. Sci. Eng. A*, 2004, vol. 382, pp. 30–34.
13. A. Rosochowski and L. Olejnik: *Mater. Sci. Forum*, 2011, vol. 674, pp. 19–28.
14. G.I. Raab, F.Z. Utyashev, R.N. Asfandiyarov, A.G. Raab, D.A. Aksenov, I.S. Kodirov, M. Janeček, and T. Krajňák: *Metals*, 2020, vol. 10, pp. 879–89.
15. M. Janeček, T. Krajňák, J. Veselý, P. Minárik, D. Preisler, J. Stráský, A.G. Raab, G.I. Raab, and R.N. Asfandiyarov: *IOP Conf. Ser. Mater. Sci. Eng.*, 2019, vol. 672, p. 012006.
16. G.I. Raab, D.A. Aksenov, R.N. Asfandiyarov, A.G. Raab, I.S. Kodirov, and M. Janeček: *Lett. Mater.*, 2019, vol. 9, pp. 494–98.
17. G. Ribárik, J. Gubicza, and T. Ungár: *Mater. Sci. Eng. A*, 2004, vols. 387–389, pp. 343–47.
18. F. Bachmann, R. Hielscher, and H. Schaeben: *Solid State Phenom.*, 2010, vol. 160, pp. 63–68.
19. H. Francillette, M. Benmaouche, and N. Gauquelin: *J. Mater. Process. Technol.*, 2008, vol. 198, pp. 86–92.
20. H.K. Lin and J.C. Huang: *Mater. Trans.*, 2002, vol. 43, pp. 2424–32.
21. T. Krajňák, P. Minárik, J. Gubicza, K. Máthis, R. Kužel, and M. Janeček: *Mater. Charact.*, 2017, vol. 123, pp. 282–93.
22. E.F. Rauch and M. Véron: *Mater. Charact.*, 2014, vol. 98, pp. 1–9.
23. A.G. Raab, D.A. Aksenov, R.N. Asfandiyarov, I.S. Kodirov, and G.I. Raab: *IOP Conf. Ser. Mater. Sci. Eng.*, 2018, vol. 447, p. 012088.
24. G. Purcek, G.G. Yapici, I. Karaman, and H.J. Maier: *Mater. Sci. Eng. A*, 2011, vol. 528, pp. 2303–2308.
25. K. Hajizadeh, B. Eghbali, K. Topolski, and K.J. Kurzydowski: *Mater. Chem. Phys.*, 2014, vol. 143, pp. 1032–38.
26. V.V. Stolyarov, Y.T. Zhu, I.V. Alexandrov, T.C. Lowe, and R.Z. Valiev: *Mater. Sci. Eng. A*, 2003, vol. 343, pp. 43–50.
27. Y.J. Chen, Y.J. Li, J.C. Walmsley, S. Dumoulin, S.S. Gireesh, S. Armada, P.C. Skaret, and H.J. Roven: *Scr. Mater.*, 2011, vol. 64, pp. 904–907.
28. C.S. Meredith and A.S. Khan: *J. Mater. Process. Technol.*, 2015, vol. 219, pp. 257–70.
29. A. Ghaderi and M.R. Barnett: *Acta Mat.*, 2001, vol. 59, pp. 7824–39.
30. Y.J. Chen, Y.J. Li, J.C. Walmsley, S. Dumoulin, P.C. Skaret, and H.J. Roven: *Mater. Sci. Eng. A*, 2010, vol. 527, pp. 789–96.
31. T. Krajňák, P. Minárik, J. Stráská, J. Gubicza, K. Máthis, and M. Janeček: *J. Alloys Compd.*, 2017, vol. 705, pp. 273–82.
32. G. Németh, K. Horváth, Ch. Hervoches, P. Cejpek, J. Palán, M. Duchek, and K. Máthis: *Metals*, 2018, vol. 8, pp. 1000–19.
33. T. Mukai, M. Yamanoi, H. Watanabe, and K. Higashi: *Scr. Mater.*, 2001, vol. 45, pp. 89–94.
34. Y. Murakami: *Metal Fatigue: Effects of Small Defects and Non-metallic Inclusions*, 2nd ed., Academic Press, Boca Raton, 2019, pp. 293–316.
35. D. Jia, Y.M. Wang, K.T. Ramesh, E. Ma, Y.T. Zhu, and R.Z. Valiev: *Appl. Phys. Lett.*, 2001, vol. 79, p. 611.
36. K.T. Park and D.H. Shin: *Metall. Mater. Trans. A*, 2002, vol. 33A, pp. 705–07.
37. Y.M. Wang and E. Ma: *Acta Mat.*, 2004, vol. 52, pp. 1699–1709.

Publisher's Note Springer Nature remains neutral with regard to jurisdictional claims in published maps and institutional affiliations.